EXTENDED MOSAIC OBSERVATIONS WITH THE COSMIC BACKGROUND IMAGER

A. C. S. Readhead,[1] B. S. Mason,[2] C. R. Contaldi,[3] T. J. Pearson,[1] J. R. Bond,[3] S. T. Myers,[4] S. Padin,[1,5]
J. L. Sievers,[1,6] J. K. Cartwright,[1,5] M. C. Shepherd,[1] D. Pogosyan,[7,3] S. Prunet,[8]
P. Altamirano,[9] R. Bustos,[10] L. Bronfman,[9] S. Casassus,[9] W. L. Holzapfel,[11]
J. May,[9] U.-L. Pen,[3] S. Torres,[10] AND P. S. Udomprasert[1]

ABSTRACT

Two years of microwave background observations with the Cosmic Background Imager (CBI) have been combined to give a sensitive, high-resolution angular power spectrum over the range $400 < l < 3500$. This power spectrum has been referenced to a more accurate overall calibration derived from the *Wilkinson Microwave Anisotropy Probe* (*WMAP*). The data cover 90 deg^2, including three pointings targeted for deep observations. The uncertainty on the $l > 2000$ power previously seen with the CBI is reduced. Under the assumption that any signal in excess of the primary anisotropy is due to a secondary Sunyaev-Zeldovich anisotropy in distant galaxy clusters, we use CBI, Arcminute Cosmology Bolometer Array Receiver, and Berkeley-Illinois-Maryland Association array data to place a constraint on the present-day rms mass fluctuation on 8 h^{-1} Mpc scales, σ_8. We present the results of a cosmological parameter analysis on the $l < 2000$ primary anisotropy data that show significant improvements in the parameters as compared to *WMAP* alone, and we explore the role of the small-scale cosmic microwave background data in breaking parameter degeneracies.

Subject headings: cosmic microwave background — cosmological parameters — cosmology: observations

1. INTRODUCTION

The Cosmic Background Imager (CBI) is a planar synthesis array designed to measure cosmic microwave background (CMB) fluctuations on arcminute scales at frequencies between 26 and 36 GHz. The CBI has been operating at its site at an altitude of 5080 m in the Chilean Andes since late 1999. Previous results have been presented by Padin et al. (2001), Mason et al. (2003), and Pearson et al. (2003). The principal observational results of these papers were the following: (1) the first detection of anisotropy on the mass scale of galaxy clusters—thereby laying a firm foundation for theories of galaxy formation; (2) the clear delineation of a damping tail in the power spectrum, best seen in the mosaic analysis of Pearson et al.; (3) the first determination of key cosmological parameters from the high-l range, independent of the first acoustic peak; and (4) the possible detection, presented in the deep field analysis of Mason et al., of power on small angular scales in excess of that expected from primary anisotropies.

The interpretation of these results has been discussed by Sievers et al. (2003) and Bond et al. (2004). The CBI data, by virtue of their high angular resolution, were able to place constraints on cosmological parameters that are largely independent of those derived from larger scale experiments; for instance, 10% measurements of Ω_{tot} and n_s using only CBI, DMR, and a weak H_0 prior. The small-scale data also play an important role in improving results on certain key parameters ($\Omega_b h^2, n_S, \tau_C$) that are less well-constrained by large-scale data.

Theoretical models predict the angular power spectrum of the CMB

$$C_l = \langle |a_{lm}|^2 \rangle, \tag{1}$$

where the a_{lm} are coefficients in a spherical harmonic expansion of temperature fluctuations in the CMB, $\Delta T/T_{CMB}$, where $T_{CMB} \approx 2.725$ K is the mean temperature of the CMB and the angle brackets denote an ensemble average. These theories also predict a series of acoustic peaks in the angular power spectrum on scales $\lesssim 1°$ ($l \gtrsim 200$) and a decline in power toward higher l due to photon viscosity and the thickness of the last scattering surface. Early indications of the first acoustic peak were presented by Miller et al. (1999); definitive measurements of the first and second peaks were reported by de Bernardis et al. (2000), Lee et al. (2001), Netterfield et al. (2002), Halverson et al. (2002), Scott et al. (2003), and Grainge et al. (2003).[12] The last of these experiments reached $l \sim 1400$. The CBI (Padin et al. 2002) has complemented these experiments by covering an overlapping range of l extending to $l \sim 3500$. The Arcminute Cosmology Bolometer Array Receiver (ACBAR; Kuo et al. 2004) has recently covered a similar range of l as the CBI at higher frequency; the Berkeley-Illinois-Maryland Association array (BIMA) has also made 30 GHz measurements at $l \sim 5000$

[1] Owens Valley Radio Observatory, California Institute of Technology, Pasadena, CA 91125.

[2] National Radio Astronomy Observatory, Green Bank, WV 24944.

[3] Canadian Institute for Theoretical Astrophysics, University of Toronto, 60 St. George Street, Toronto, Ontario, M5S 3H8, Canada.

[4] National Radio Astronomy Observatory, Socorro, NM 87801.

[5] Current address: University of Chicago, 5640 South Ellis Avenue, Chicago, IL 60637.

[6] Current address: Canadian Institute for Theoretical Astrophysics, University of Toronto, 60 St. George Street, Toronto, Ontario, M5S 3H8, Canada.

[7] Department of Physics, University of Alberta, Edmonton, Alberta T6G 2J1, Canada.

[8] Institut d'astrophysique de Paris, 98bis, Boulevard Arago, 75014 Paris, France.

[9] Departamento de Astronomía, Universidad de Chile, Casilla 36-D, Santiago, Chile.

[10] Departamento de Ingeniería Eléctrica, Universidad de Concepción, Casilla 160-C, Concepción, Chile.

[11] University of California, 366 LeConte Hall, Berkeley, CA 94720-7300.

[12] In the parameter analysis of § 4 we use the latest VSA data (Dickinson et al. 2004), which were released shortly after this paper was first submitted.

that probe the secondary Sunyaev-Zeldovich effect (SZE) anisotropy (Dawson et al. 2002). These experiments, which employ a wide variety of instrumental and experimental techniques, present a strikingly consistent picture that supports inflationary expectations (see Bond et al. 2002 for a review). However, the results at intermediate angular scales ($500 < l < 2000$) currently have comparatively poor l-space resolution, and the high-l results are difficult to compare conclusively owing to the low signal-to-noise ratio ($\sim 2-4$). The results presented here improve the situation by (1) expanding the coverage of the CBI mosaics for higher l resolution, (2) integrating further on the deep fields, and (3) combining the deep and mosaic data for a single power spectrum estimate over the full range of l covered by the CBI.

The CBI results presented by Mason et al. (2003) and Pearson et al. (2003) were based on data obtained between January and December of 2000. Mason et al. analyzed the data resulting from extensive integration on three chosen "deep fields" to constrain the small-scale signal; the analysis of Pearson et al. used data with shallower coverage of a larger area ("mosaics") to obtain better Fourier-space resolution. Further observations were conducted during 2001; these were used to extend the sky coverage of the mosaics in order to attain higher resolution in l and to go somewhat deeper on the existing deep fields. This paper presents the power spectrum resulting from the combination of the full CBI primary anisotropy data set, which comprises data from years 2000 and 2001 on both mosaic *and* deep fields. Two of the mosaic fields (14 and 20 hr) include deep pointings; there is also a third deep pointing (08 hr), and a third mosaic (02 hr). The CBI data have been recalibrated to a more accurate power scale derived from the *Wilkinson Microwave Anisotropy Probe* (*WMAP*).

The organization of this paper is as follows. In § 2 we discuss the observations and *WMAP*-derived recalibration. In § 3 we present images and power spectra derived from the data and explain the methodology employed in their derivation. In § 4 we use these results to constrain cosmological parameters based on standard models for primary and secondary CMB anisotropies. We present our conclusions in § 5.

2. OBSERVATIONS AND CALIBRATION

The analysis in this paper includes data collected in the year 2001 in addition to the year 2000 data previously analyzed. In January through late March of 2001 there was an unusually severe "Bolivian winter," which prevented the collection of useful data; regular observations resumed on 2001 March 28 and continued until 2001 November 22. The weather in the austral winter of 2001 was considerably less severe than it had been in 2000, so that less observing time was lost due to poor weather.

In 2001 we concentrated primarily on extending the mosaic coverage in three fields in order to obtain higher resolution in l. We also made a small number of observations in the deep fields discussed by Mason et al. (2003). The original field selection is discussed by Mason et al. (2003) and Pearson et al. (2003). Since our switching strategy employs pairs of fields separated in the east-west direction, contiguous extensions were easiest in the north-south direction. The extensions to these fields were selected to minimize point-source contamination. In two cases (the 02 and 14 hr fields) this procedure resulted in extensions to the north and in one case (20 hr) in an extension to the south. The images for the combined 2000+2001 mosaic observations are shown in Figure 1, and the sensitivity maps are shown in

Figure 2. The total areas covered are 32.5, 3.5, 26.2, and 27.1 deg^2 for the 02, 08, 14, and 20 hr fields, respectively.[13]

The CBI two-year data were calibrated in the same manner as the first-year data (Mason et al. 2003), except that the overall calibration scale has been adjusted in light of the recent *WMAP* observations of Jupiter (Page et al. 2003). The flux density scale for the first-year data was determined from the absolute calibration measurements by Mason et al. (1999), which gave a temperature for Jupiter at 32 GHz of $T_J = 152 \pm 5$ K (note that all planetary temperatures discussed in this paper are the Rayleigh-Jeans brightness temperature of the planet minus the Rayleigh-Jeans temperature of the CMB at the same frequency). Page et al. (2003) have determined $T_J(32 \text{ GHz}) = 146.6 \pm 2.0$ K from measurements relative to the CMB dipole. Figure 3 shows measurements of Jupiter with the CBI on the old (Mason et al. 1999) calibration scale, as well as the *WMAP* measurements. The slopes of the CBI and *WMAP* spectra are in agreement to better than 1 σ, and the 32 GHz values are also within 1 σ; these results support the original CBI amplitude and spectral slope calibrations. Since the *WMAP* and Mason et al. measurements are independent we adopt a weighted mean of the two and base the CBI calibration on $T_J(32 \text{ GHz}) = 147.3 \pm 1.8$ K. This 3% reduction in the CBI flux density scale corresponds to an overall scaling down of the CBI power spectrum by 6% in power. This scaling is consistent with the original 3.5% flux density scale uncertainty (7% in power). The new CBI calibration has an uncertainty of 1.3% in flux density (2.6% in power).

3. DATA ANALYSIS

The basic methods of CBI data analysis and spectrum extraction are described fully by Mason et al. (2003), Pearson et al. (2003), and Myers et al. (2003). The primary differences in this analysis are: an improved estimate of the thermal noise, which has allowed us to bring the mosaic data to bear on the "high-l excess" evident in the deep data; new data cuts needed to deal with point sources in the mosaic extensions; and a revised l-binning appropriate to the expanded sky coverage and variable noise level of the new data. These aspects of the analysis, and the resulting power spectrum, are described in the following subsections.

3.1. *Thermal Noise Estimates*

We estimate the thermal noise variance for each uv data point in each scan of the CBI data set by the mean-squared deviation about the mean, and subsequently use a weighted average to combine the estimates from different scans. It is necessary to make a small correction to the estimated variance for each uv data point due to the finite number of samples that enter the estimate. Mason et al. (2003) present simple analytic arguments placing this correction at 8% in variance and estimate a 2% uncertainty in the variance. We have since improved our estimate of the CBI thermal noise variance resulting in a variance correction factor of 1.05 ± 0.01. This is 1.5 σ from the factor (1.08 ± 0.02) applied to the year 2000 data; the overestimate of noise in Mason et al. will have caused a slight underestimate—by 42 μK^2—of the excess power level at high l in the original CBI deep result (Mason et al. 2003).

We calculated the noise variance correction in several ways: a first-order analytic calculation of the noise distribution; a

---

[13] These are the areas, counting LEAD and TRAIL fields separately, mapped to an rms sensitivity of 10 mJy beam^{-1} or better.
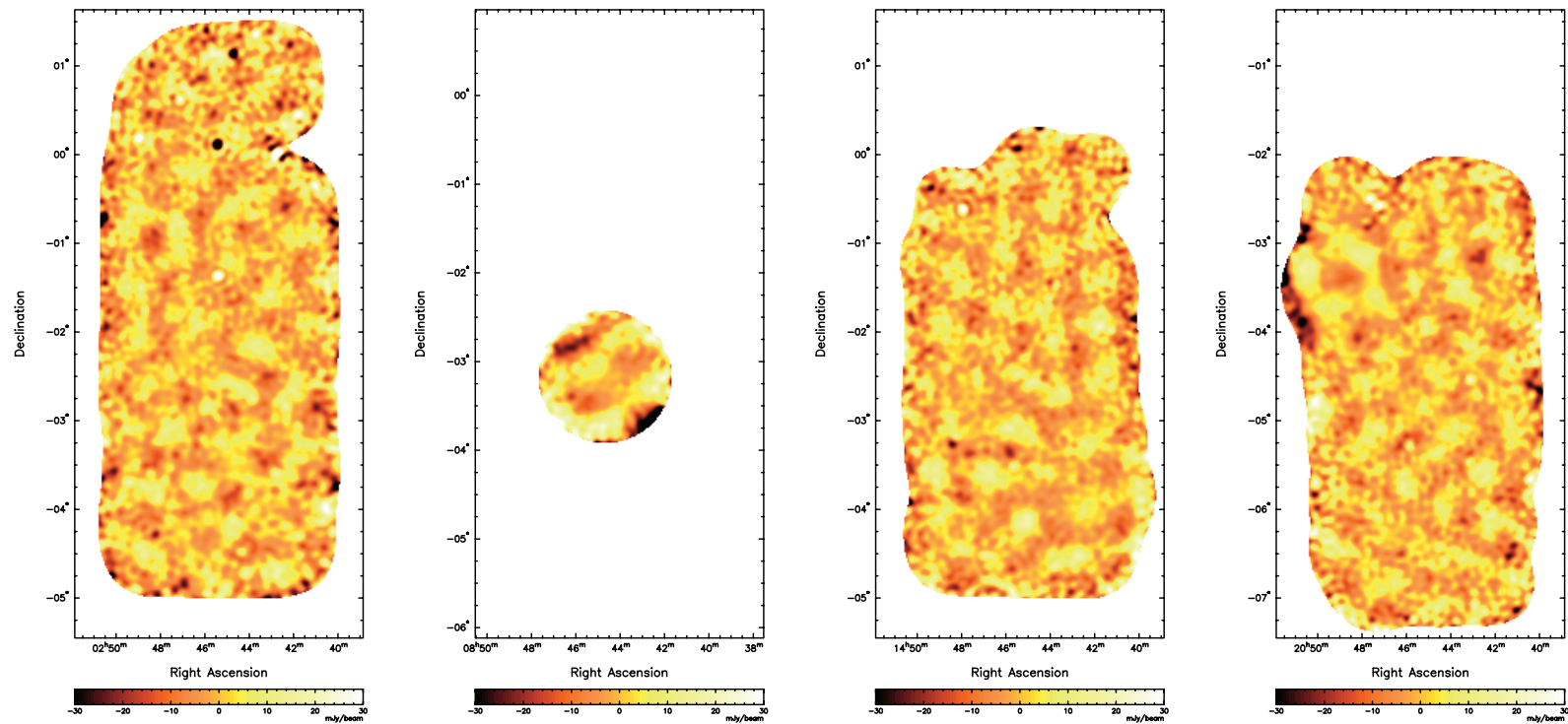
Fig. 1.—Extended mosaic images from the combined 2000+2001 observations. The angular resolution of these observations is ~5′ (FWHM).
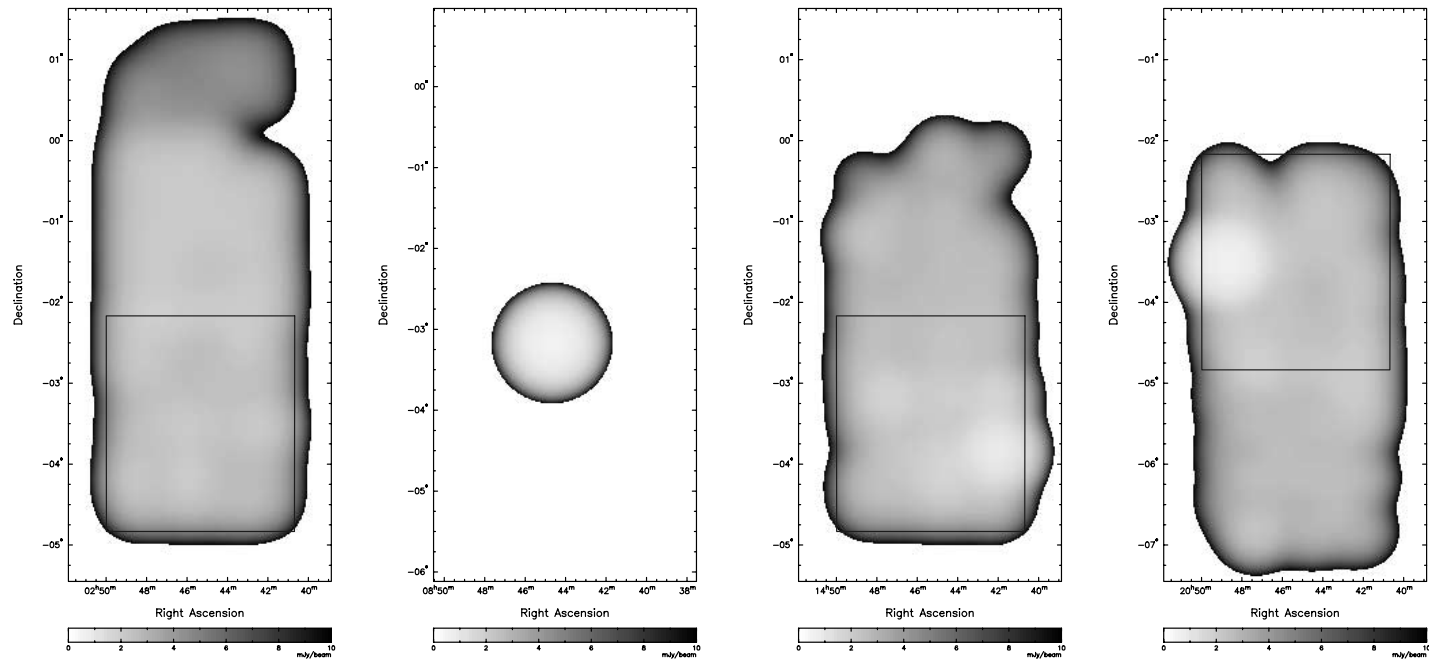
FIG. 2.—Sensitivity across the extended mosaic images from the combined 2000+2001 observations. The deep pointings within the 14 and 20 hr mosaic fields are evident in the bottom right and upper left of the third and fourth panels, respectively. Blue boxes indicate the approximate regions covered in the earlier CBI mosaic analysis of Pearson et al. (2003).
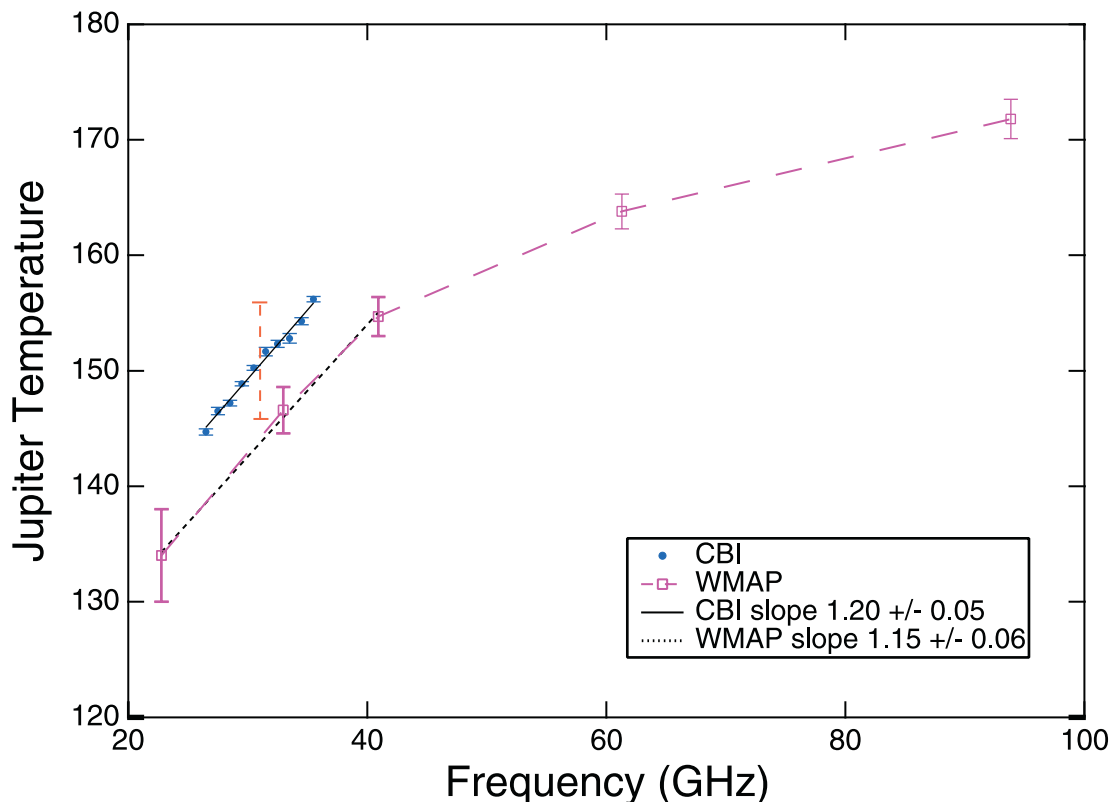
Fig. 3.—Comparison of Jupiter temperatures measured with the CBI and with *WMAP*. The spectrum of Jupiter in this frequency range is not thermal owing to an absorption feature. The individual channel CBI temperatures of Jupiter in the 26–36 GHz range are shown by the filled blue circles, and those of *WMAP* in the range 22–94 GHz are shown by the open pink squares. The dotted and solid lines, respectively, show the best-fit slopes to *WMAP* and CBI data over the 20–40 GHz range. The CBI temperatures shown here were determined assuming $T_J(32\ \mathrm{GHz}) = 152 \pm 5\mathrm{K}$ (Mason et al. 1999); the systematic error bar on this calibration is shown as a dotted red line. The *WMAP* error bars include both random and systematic errors.

numerical (fast-Fourier transform [FFT] based) integration of the distribution; and analysis of simulated data. The simulations use the actual CBI data as a starting point, replacing each 8.4 s integration with a point drawn from a Gaussian distribution of zero mean with a dispersion derived from the estimated statistical weight of the data point. This method accounts for variations in the statistical weight from baseline to baseline and variations in the number of data points per scan due, for instance, to rejected data. This gives a result of 1.044 ± 0.002 (statistical error). The FFT calculation agrees within the 0.2% uncertainty in the variance. The first-order analytic calculation is lower by 0.6% but should be considered to be only a crude check. Details of the noise variance estimate are presented by Sievers (2003).

The simulations were analyzed entirely in the visibility domain. As a further check on the variance correction calculations, we gridded the visibility data following the procedure used in analyzing the real CBI data (Myers et al. 2003). Monte Carlo calculations of the χ^2 of the gridded estimators (using the inverse of the full noise matrix) yield a noise correction factor of 1.050 ± 0.004 (statistical error). This is why we adopt a value of 1.05, since it is the gridded estimators that are used in the power spectrum estimation. We conservatively adopt a 1% uncertainty in the variance correction although the level of agreement between different methods of estimating this is ~0.5%.

The importance of the improved accuracy of the thermal noise calculation is illustrated by considering the year 2000 CBI data at $l > 2000$. Referenced to the current calibration and noise scale, the year 2000 mosaic data presented by Pearson

et al. (2003) yield a band power of $206 \pm 178\ \mu\mathrm{K}^2$. We considered combining these data with the year 2000 CBI deep field data (Mason et al. 2003). The thermal noise variance in this last bin for the year 2000 mosaic, however, is $4307\ \mu\mathrm{K}^2$, which yields a $86\ \mu\mathrm{K}^2$ systematic uncertainty due to the thermal noise variance correction alone given the previous 2% uncertainty in the noise variance. The thermal noise variance in the year 2000 deep field data is $1293\ \mu\mathrm{K}^2$, resulting in a $26\ \mu\mathrm{K}^2$ uncertainty due to the noise estimate; this was substantially less than the greatest systematic uncertainty, the residual point-source correction at $50\ \mu\mathrm{K}^2$. It was clear that the mosaic data would contribute little to our understanding of the signal at $l > 2000$. In contrast, the thermal noise variance for the 2000+2001 mosaic+deep data in the last ($l > 1960$) bin is $2054\ \mu\mathrm{K}^2$, which with our present 1% knowledge of the noise variance results in a contribution to the systematic error budget slightly lower than that from noise in the year 2000 deep data and subdominant to the residual point-source contribution.

3.2. *Treatment of the Discrete Source Foreground*

The treatment of the discrete source foreground is similar to that adopted in the earlier CBI analyses of Mason et al. (2003) and Pearson et al. (2003). All sources above 3.4 mJy in the 1.4 GHz NRAO VLA Sky Survey (NVSS; Condon et al. 1998) were included in a constraint matrix and projected out of the data (Bond, Jaffe, & Knox 1998; Halverson et al. 2002). This is roughly equivalent to completely down-weighting the synthesized beam corresponding to *each* of these sources and effectively eliminates 25% of our data. We correct for sources below the 3.4 mJy cutoff in NVSS statistically. The statistical
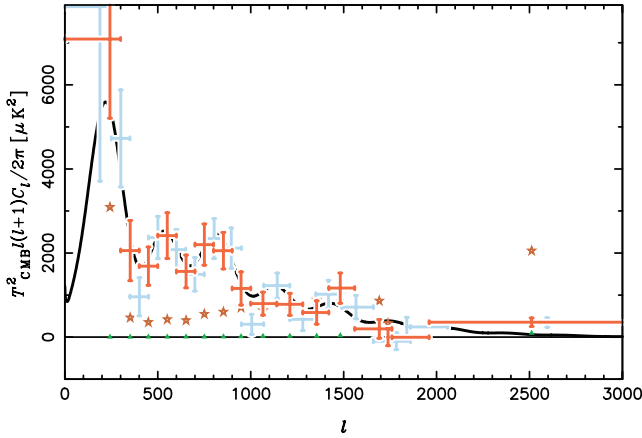
FIG. 4.—The 2000+2001 CBI spectrum. The "even" binning is shown in red and the "odd" binning in light blue. Orange stars indicate the thermal noise variance; green triangles indicate the statistical source correction which has been subtracted from the power spectrum. The solid black line is the *WMAP* ΛCDM model with a pure power-law primordial spectrum (model spectrum is file wmap_lcdm_pl_model_yr1_v1.txt, available on the *WMAP* World Wide Web site, http://lambda.gsfc.nasa.gov).

correction reduces the power in the high-*l* bin by ∼20% (see Fig. 4). We have also obtained independent 30 GHz measurements of the bright sources in the CBI fields with the Owens Valley Radio Observatory (OVRO) 40 m telescope. For presentation purposes we subtract these flux densities from the maps with reasonable results, although some residuals are visible. The constraint matrices eliminate the impact of any errors in the source subtraction, and the power spectrum results are unchanged even if no OVRO subtraction is performed.

Although the extensions were chosen to minimize point-source contamination, the larger size of the expanded mosaics and the requirement that the extensions be contiguous with the already highly optimized original CBI mosaic fields resulted in a handful of sources brighter than those present in the year 2000 CBI mosaic data (Pearson et al. 2003). In particular, the 2 hr extension contains the Seyfert galaxy NGC 1068

$(S_{30\,\mathrm{GHz}} \sim 0.4\,\mathrm{Jy})$ that we found was not effectively removed by the constraint matrix. To deal with this we excluded CBI pointings around this source (as well as one other bright source in the 2 hr field, and one in each of the 14 hr field and 20 hr fields) until the maximum signal-to-noise ratio on *any* discrete source in the total mosaic areas—before subtraction or projection—was less than some threshold *X*. In our final analysis we have adopted $X = 50$, eliminating nine of 263 CBI pointings. To check this we analyzed the data with a more stringent signal-to-noise ratio cutoff of $X = 25$ and found no significant change in the power spectrum.

3.3. *Power Spectrum Analysis*

The data set combines very deep pointings (and thus low noise levels) on a few small areas with substantially shallower coverage of wider areas. The signal at low-*l* is stronger and the features in the power spectrum are expected to be more distinct, so we seek to use the wider coverage for maximum *l* resolution on large angular scales. Most of the statistical weight in the data set at small scales comes from the deep integrations, and since the sky coverage of these is quite limited, the *l* resolution is lower. In this regime the signal-to-noise ratio is lower and we seek to compensate by combining many Fourier modes. In order to present a single unified power spectrum that makes use of information from all the data over the full range of angular scales, we adopt bins that are narrowest at low *l* ($\delta l = 100$) and increase in steps toward a single high-*l* bin above $l \sim 2000$. The bin widths were chosen to yield maximum *l* resolution while keeping typical bin-to-bin anti-correlations to less than ∼30%. We have chosen two distinct binnings of the data, which we call the "even" and "odd" binnings. These binnings are not independent but are helpful in determining whether particular features are artifacts of the bin choice. Subsequent statistical analyses—including primary anisotropy parameter estimation and the σ_8 analysis of secondary anisotropy—employ only one binning (the "even" binning).

The updated CBI power spectrum is shown in Figure 4 and tabulated in Table 1. Results are presented in terms of band

TABLE 1
CBI BAND-POWER MEASUREMENTS

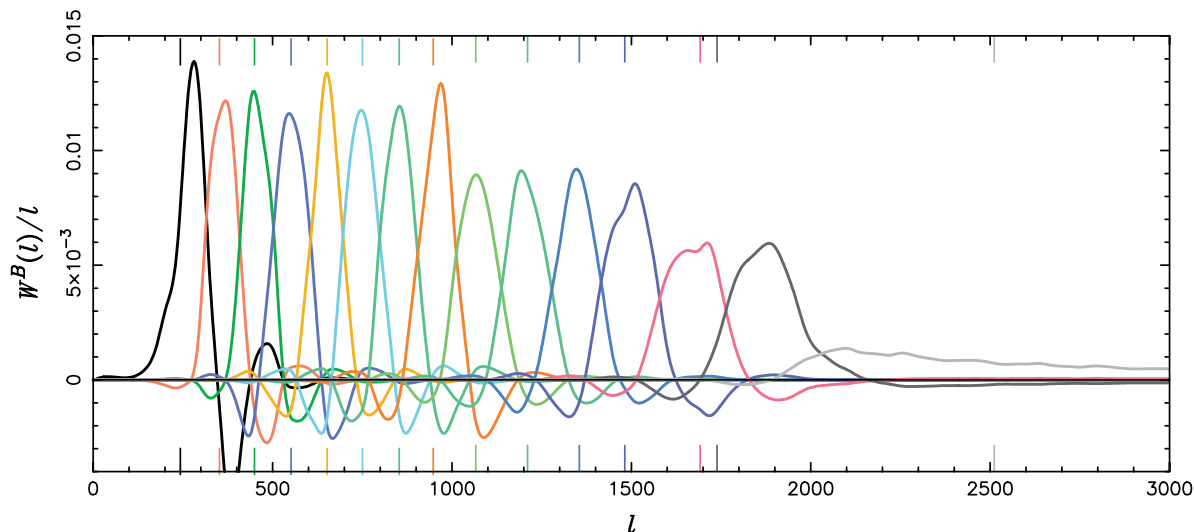|	EVEN BINNING			ODD BINNING		
BIN	*l*-Range	Band Power (μK^2)	X_B (μK^2)	*l*-Range	Band Power (μK^2)	X_B (μK^2)
1.....................	0–300	7091 ± 1882	3176	0–250	7860 ± 4151	8196
2.....................	300–400	2059 ± 717	489	250–350	4727 ± 1157	796
3.....................	400–500	1688 ± 457	377	350–450	961 ± 454	397
4.....................	500–600	2415 ± 545	449	450–550	2369 ± 504	390
5.....................	600–700	1562 ± 391	423	550–650	2081 ± 480	455
6.....................	700–800	2201 ± 490	577	650–750	1494 ± 400	460
7.....................	800–900	2056 ± 436	631	750–850	2346 ± 476	582
8.....................	900–1000	1158 ± 396	743	850–950	2117 ± 482	770
9.....................	1000–1140	797 ± 275	674	950–1070	305 ± 239	636
10...................	1140–1280	780 ± 263	726	1070–1210	1226 ± 300	694
11...................	1280–1420	586 ± 278	933	1210–1350	423 ± 269	820
12...................	1420–1560	1166 ± 361	1064	1350–1490	1020 ± 333	1040
13...................	1560–1760	196 ± 223	941	1490–1660	714 ± 279	960
14...................	1760–1960	-4 ± 203	386	1660–1860	-98 ± 201	834
15...................	1960+	355 ± 103	2184	1860–2060	243 ± 229	457
16...................	...	...	...	2060+	346 ± 113	2385

Fig. 5.—The 2000+2001 CBI window functions ("even" binning).

power ($\Delta T^2 = T^2_{\mathrm{CMB}} l(l+1)C_l/2\pi$), which is assumed to be flat within each bin; also shown are the values of the noise power spectrum X_B. This table presents both "even" and "odd" binnings of the CBI data. Window functions for the two binnings are presented in Figures 5 and 6. The procedures for calculating window functions and noise power spectra are defined by Myers et al. (2003).

The possible detection of power in excess of the expected primary anisotropy at high-l by Mason et al. (2003) has stirred considerable interest (e.g., Komatsu & Seljak 2002; Oh et al. 2003; Subramanian et al. 2003; Griffiths et al. 2003), and the results that we present in this paper improve the band-power constraint. Binning all the 2000+2001 data above $l = 1960$ together, we find a band power of $355 \pm 103\ \mu\mathrm{K}^2$ (random error only). By way of comparison, the Mason et al. result, referenced to the current CBI calibration scale and noise correction, is $511 \pm 156\ \mu\mathrm{K}^2$; the new result is thus 25% lower but within $\sim 1\ \sigma$ of the Mason et al. result, although the data sets are not independent. Table 2 presents the $l > 2000$ band-power constraints from these and three other combinations of

the full CBI data set, all referenced to the current calibration scale and with our best noise variance estimates. For purposes of comparison this table shows only the random errors derived from the Fisher matrix at the best-fit point (which includes couplings to other bins); in addition there is a common overall uncertainty of $48\ \mu\mathrm{K}^2$ from the discrete source correction.

In order to constrain the excess more accurately we have explicitly mapped the likelihood in the last bin, allowing for the following systematic errors in the analysis: uncertainty in the statistical source correction ($48\ \mu\mathrm{K}^2$); uncertainty in the thermal noise power spectrum ($20\ \mu\mathrm{K}^2$); and the $56\ \mu\mathrm{K}^2$ dispersion in the high-l band power caused by the uncertainty in the band power of the neighboring bin.[14] We determine confidence intervals on ΔT^2 of 233–492 $\mu\mathrm{K}^2$ (68%) and 110–630 $\mu\mathrm{K}^2$ (95%). From the 68% confidence limit we can state our result as $355^{+137}_{-122}\ \mu\mathrm{K}^2$. This result is consistent with but

[14] The error quoted from the Fisher matrix at the best-fit point, $\pm 103\ \mu\mathrm{K}^2$, includes this contribution, and it is only added in separately here because the likelihood mapping procedure keeps other bins fixed.
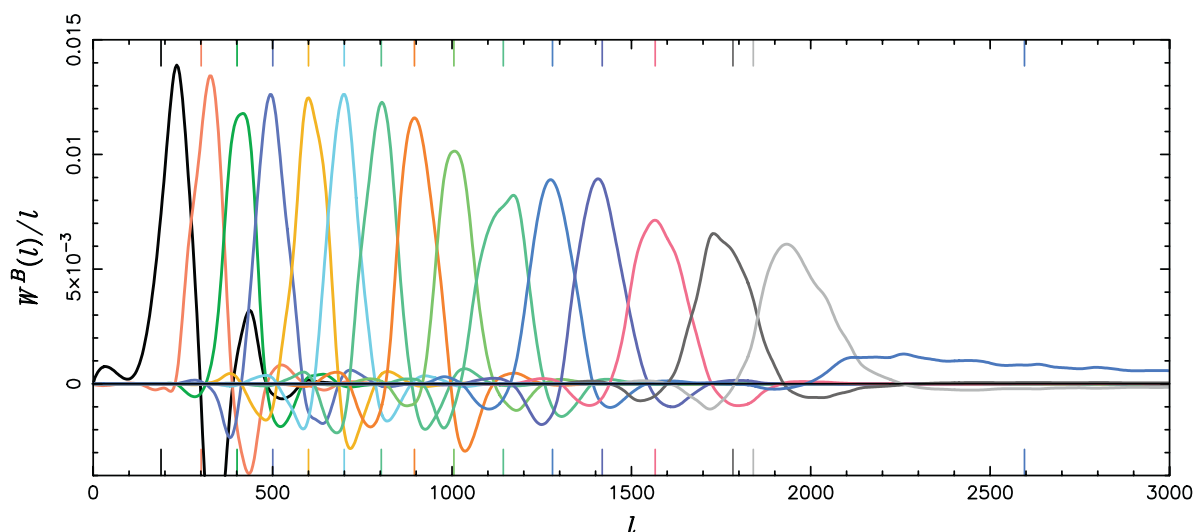

Fig. 6.—The 2000+2001 CBI window functions ("odd" binning).

TABLE 2

Comparison of High-l Results for Different Subsets
of CBI Data

Data Set	Band Power (μK^2)
2000+2001 Deep+Mosaic..........................	355 ± 103
2000+2001 Deep....................................	393 ± 134
2000 Deep...	514 ± 158
2000 Deep+Mosaic.................................	457 ± 122
2000 Mosaic	206 ± 178

Notes.—Results for the high-l bin on the *WMAP* power scale, with current noise correction applied. For further discussion see text.

lower than that derived from the earlier analysis of CBI deep fields, and while the detection of power remains statistically significant, the detection of power in excess of the band-averaged power expected from the primary anisotropy ($\sim$80–90 μK^2) is marginal. A slightly more significant detection is obtained by combining CBI, ACBAR, and BIMA data, and we present the results of such an analysis in § 4.3.

We have also computed the value of the high-l bin for several statistically independent splits of the total (2000+2001 deep plus mosaic) data set. In all cases the power spectra are consistent. The most sensitive of these splits was a division of the data set into two halves by field (2 hr plus 8 hr, and 14 hr plus 20 hr), in which case the high-l band powers were within 1.3 σ of each other and consistent with the best value of 355 μK^2.

4. INTERPRETATION

4.1. *Basic Cosmological Parameters from the Primary Anisotropy*

We use a modified version of the publicly available Markov Chain Monte Carlo (MCMC) package COSMOMC[15] (Lewis & Bridle 2002) to obtain cosmological parameter fits to the CMB data. The code has been tested extensively against our fixed-resolution grid-based method, which we applied to the first year CBI data in the papers by Sievers et al. (2003) and Bond et al. (2004). Bond et al. (2003) show that the agreement

[15] See http://cosmologist.info/cosmomc.

between the two methods is good when identical data and priors are used. Advantages of the MCMC method include a reduced number of model spectrum computations required to accurately sample the multidimensional likelihood surfaces and automatic rather than built-in adaptivity of the parameter sets sampled.

Our typical run involves the calculation of eight Markov chains over the following basic set of cosmological parameters: $\omega_b \equiv \Omega_b h^2$, the physical density of baryons; $\omega_c \equiv \Omega_c h^2$, the physical density of cold dark matter; Ω_Λ, the energy density in the form of a cosmological constant; n_s, the spectral index of the scalar perturbations; A_s, an amplitude parameter for the scalar perturbations; and τ_C, the optical depth to the surface of last scattering. Each chain is run on a separate 2-CPU node of the CITA McKenzie Beowulf cluster for a typical run time of approximately 9 hr when the proposal densities are estimated using a previously computed covariance matrix for the same set of parameters. The chains are run until the largest eigenvalue returned by the Gelman-Rubin convergence test reaches 0.1. We run the chains at a temperature setting of 1.2 in order to sample more densely the tails of the distributions; the samples are adjusted for this when analyzing the chains.

All of our parameter analysis imposes a "weak-h" prior comprising limits on the Hubble parameter (45 km s^{-1} Mpc^{-1} < H_0 < 90 km s^{-1} Mpc^{-1}) and the age of the universe ($t_0 > 10$ Gyr). We primarily consider flat models ($\Omega_{tot} = 1$) in this work, and unless otherwise stated a flat prior has been imposed. Within the context of flat models the weak-h prior influences the results very little. We include all of the band powers shown in Table 1 except for the highest and lowest l bands. The highest band is excluded due to possible contamination by secondary anisotropies; the first band is poorly constrained and provides no useful information.

In Table 3 we compare the constraints obtained when including only the *WMAP* measurements with those obtained when also including the new CBI band powers and a compilation of "ALL" present CMB data[16] for the weak-h prior case. We include both total intensity and TE spectra from *WMAP* in our analysis. For BOOMERANG and ACBAR, recalibrations and their uncertainties were applied using the power spectrum based method described in Bond et al. (2003), which

[16] *WMAP* (Bennett et al. 2003); VSA (Dickinson et al. 2004); DASI (Halverson et al. 2002); ACBAR (Kuo et al. 2004); MAXIMA (Lee et al. 2001); and BOOMERANG (Ruhl et al. 2003).

TABLE 3

Cosmological Constraints from the "*WMAP* Only," "CBI+*WMAP*," and
"CBI+All" for an Assumed $\Omega_{\text{tot}} = 1.0$.

Parameter	*WMAP* only	CBI+*WMAP*	CBI+ALL
$\Omega_b h^2$	$0.0243^{+0.0016}_{-0.0016}$	$0.0225^{+0.0011}_{-0.0011}$	$0.0225^{+0.0009}_{-0.0009}$
$\Omega_c h^2$	$0.123^{+0.017}_{-0.018}$	$0.107^{+0.012}_{-0.013}$	$0.111^{+0.010}_{-0.009}$
Ω_Λ...	$0.71^{+0.08}_{-0.08}$	$0.75^{+0.05}_{-0.05}$	$0.74^{+0.05}_{-0.04}$
τ_C	$0.18^{+0.03}_{-0.06}$	$0.13^{+0.02}_{-0.04}$	$0.11^{+0.02}_{-0.03}$
n_s	$1.01^{+0.05}_{-0.05}$	$0.96^{+0.03}_{-0.03}$	$0.95^{+0.02}_{-0.02}$
$10^{10}A_s$...................................	$27.7^{+5.5}_{-5.1}$	$22.2^{+2.8}_{-2.9}$	$21.9^{+2.4}_{-2.3}$
H_0	$72.1^{+6.4}_{-5.8}$	$73.4^{+4.6}_{-4.7}$	$71.9^{+3.9}_{-3.9}$
Age (Gyr)..............................	$13.3^{+0.3}_{-0.3}$	$13.7^{+0.2}_{-0.3}$	$13.7^{+0.2}_{-0.2}$
Ω_m..	$0.29^{+0.08}_{-0.08}$	$0.25^{+0.05}_{-0.05}$	$0.26^{+0.04}_{-0.05}$
σ_8..	$0.96^{+0.14}_{-0.15}$	$0.78^{+0.08}_{-0.08}$	$0.80^{+0.06}_{-0.06}$

Notes.—We included weak external priors on the Hubble parameter (45 km s^{-1} Mpc^{-1} < H_0 < 90 km s^{-1} Mpc^{-1}) and the age of the universe ($t_0 > 10$ Gyr). The flatness prior has the strongest effect on the parameters by breaking the geometrical degeneracy and allowing us to derive tight constraints on H_0 and Ω_m.
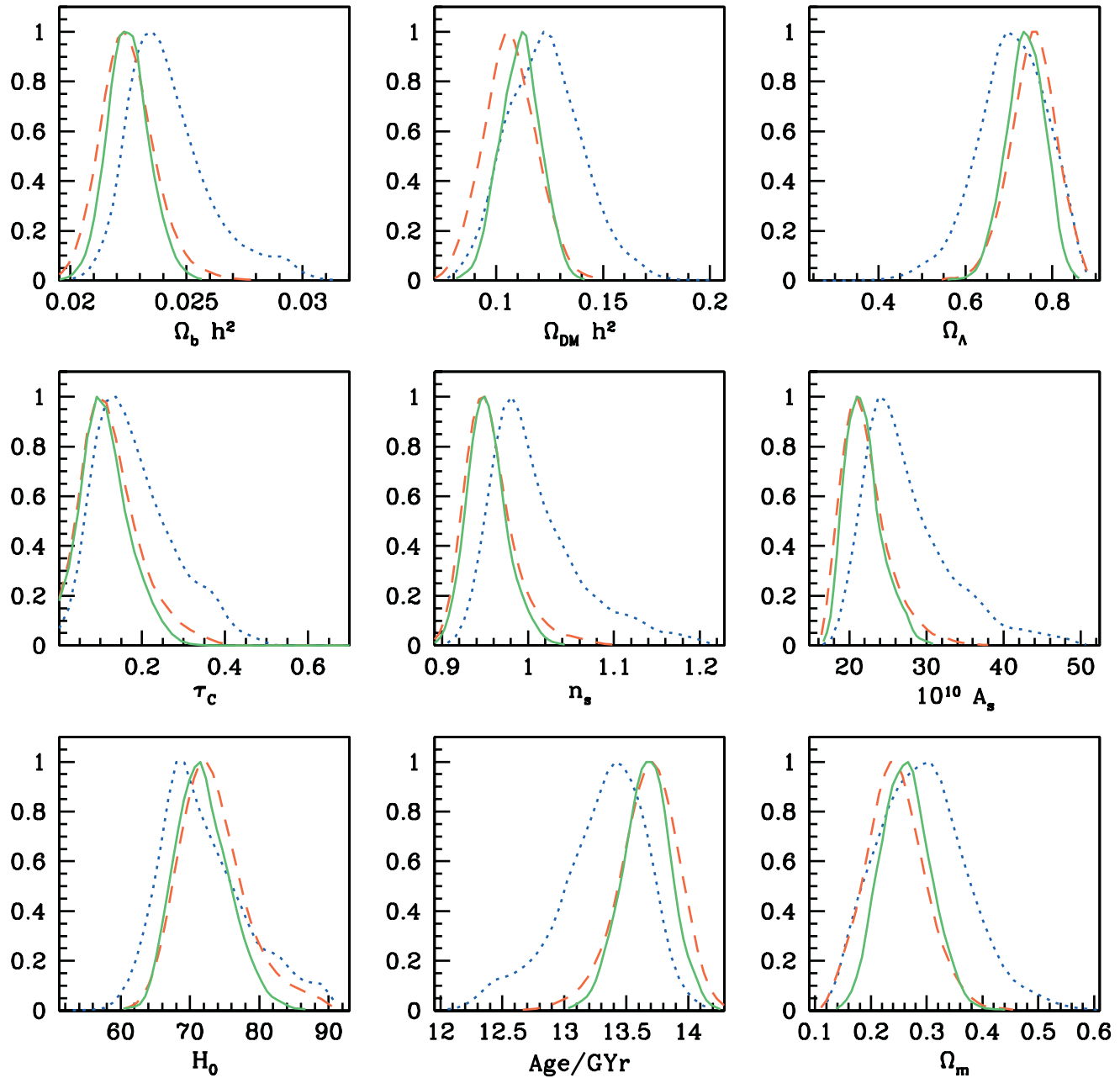
Fig. 7.—Marginalized likelihood curves for a range of individual cosmological parameters, each shown for three CMB data sets: "*WMAP* only" (*blue dotted line*); "CBI+*WMAP*" (*red dashed line*); and "CBI+ALL" (*green solid line*). In all cases a flat plus weak-*h* prior is used.

obtains maximum likelihood calibration parameters as a by-product of the optimal, combined power spectrum calculation with multiple experiment results. Detailed results for the fits are summarized in Table 1 of Bond et al. (2003). We note that this method gives calibrations in agreement with those obtained from the *WMAP*/CBI cross-calibration via Jupiter, and a map-based comparison of BOOMERANG and *WMAP* gives a very similar recalibration and error for BOOMERANG to those used here (E. Hivon 2003, private communication). The original reported calibrations of DASI, Maxima, and VSA were used. Although the optimal spectrum procedure also produces best-fit values with errors for the beam parameters of each experiment, we have used the reported beams and their uncertainties in each case for the parameter estimates given in this paper.

The "CBI+ALL" parameters and their errors in Table 3 can be compared with the "March 2003" values given in Table 5 of Bond et al. (2003). These were evaluated using the MCMC method with the calibrations for CBI used here, but no recalibration with decreased errors for BOOMERANG and ACBAR. The results are quite similar.

Our main results for the flat plus weak-*h* case are summarized in Figure 7 showing marginalized one-dimensional distributions for the basic six parameters together with three other derived parameters: the Hubble parameter H_0 in units of km s^{-1} Mpc^{-1}, the total age t_0 of the universe in gigayears, and the total energy density of matter Ω_m in units of the critical energy density. We show three curves for each parameter corresponding to the "*WMAP* only," "CBI+*WMAP*," and "CBI+ALL" cases. They show how the inclusion of high-*l* band
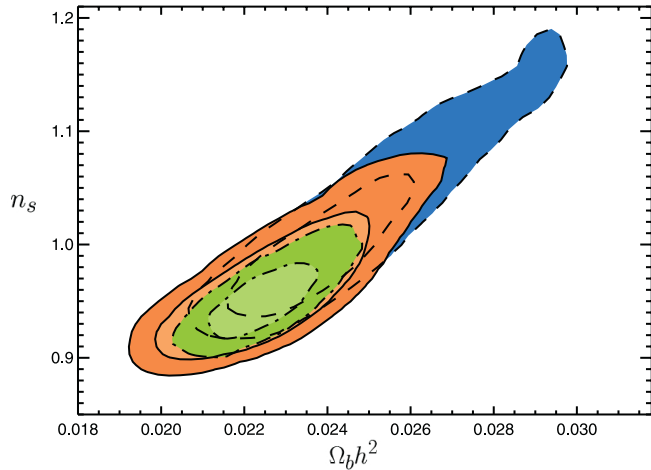
FIG. 8.—CMB constraints on $\Omega_b h^2$ and n_s, marginalized over other parameters. Shown are the 1 and 2 σ constraints from: "*WMAP* only" (*dashed lines delineating the blue region*); "*WMAP*+CBI" (*solid lines delineating the orange region*); "CBI+ALL" (*dash-dotted lines delineating the green regions*). In all cases a flat plus weak-*h* prior is used.

FIG. 9.—CMB constraints on τ_C and σ_8, marginalized over other parameters. Shown are the 1 and 2 σ constraints from: "*WMAP* only" (*dashed lines delineating the blue region*); "*WMAP*+CBI" (*solid lines delineating the orange region*); "CBI+ALL" (*dash-dotted lines delineating the green regions*). In all cases a flat plus weak-*h* and LSS priors are included. Only data at $l < 2000$ is used in this analysis, although the σ_8 results are consistent with constraints from the high-*l* analysis of secondary SZE anisotropy.

powers is crucial to excluding significant tails in the distributions that remain because of the limited *l*-range of the *WMAP* results.

Of particular significance is the effect of including the CBI band powers on the correlated trio n_s, τ_C, and ω_b. The "*WMAP* only" case shows long tails toward high values for the three parameters that are excluded only when the CBI or the "CBI+ALL" combinations are included. We do not include a cutoff on the value of τ_C, as was done by Spergel et al. (2003). Their cutoff has a rather strong effect also on the tails of the distribution in n_s and ω_b. We rely only on the addition of extra data. This can be seen in Figure 8, which shows the marginalized distribution in the n_s-ω_b plane for the "*WMAP* only," "CBI+*WMAP*," and "CBI+ALL" cases.

The results of the CMB+LSS parameter analyses are presented in Table 4. We consider two cases to illustrate the impact of large scale structure observations on the cosmological parameter distributions: (1) the Two Degree Galaxy Redshift Survey (2dfGRS) results of Percival et al. (2002) and (2) a more conservative LSS prior that straddles most weak lensing and cluster results for the amplitude σ_8 (Bond et al. 2003 and references therein), but a weaker version of the 2dFGRS

TABLE 4
Cosmological Constraints from "CBI+All" Data
Plus LSS Constraints

Parameter	CBI+ALL+2df	CBI+ALL+LSS
$\Omega_b h^2$	$0.0224^{+0.0008}_{-0.0008}$	$0.0225^{+0.0009}_{-0.0008}$
$\Omega_c h^2$	$0.117^{+0.007}_{-0.006}$	$0.118^{+0.007}_{-0.007}$
Ω_Λ	$0.71^{+0.03}_{-0.03}$	$0.71^{+0.03}_{-0.04}$
τ_C	$0.10^{+0.02}_{-0.02}$	$0.11^{+0.02}_{-0.0}$
n_s	$0.95^{+0.02}_{-0.02}$	$0.95^{+0.02}_{-0.02}$
$10^{10}A_S$	$21.6^{+2.1}_{-2.0}$	$22.3^{+2.1}_{-2.2}$
H_0	$69.6^{+2.5}_{-2.5}$	$69.6^{+2.8}_{-2.9}$
Age (Gyr)	$13.7^{+0.2}_{-0.2}$	$13.7^{+0.2}_{-0.2}$
Ω_m	$0.29^{+0.03}_{-0.03}$	$0.29^{+0.04}_{-0.03}$
σ_8	$0.82^{+0.05}_{-0.05}$	$0.83^{+0.05}_{-0.05}$

Notes.—The priors are the same as in Table 3. In addition we have added a LSS prior in the form either of constraints on the combination $\sigma_8 \Omega_m^{0.56}$ and the shape parameter $\Gamma_{\rm eff}$, or using the 2dfGRS power spectrum results.
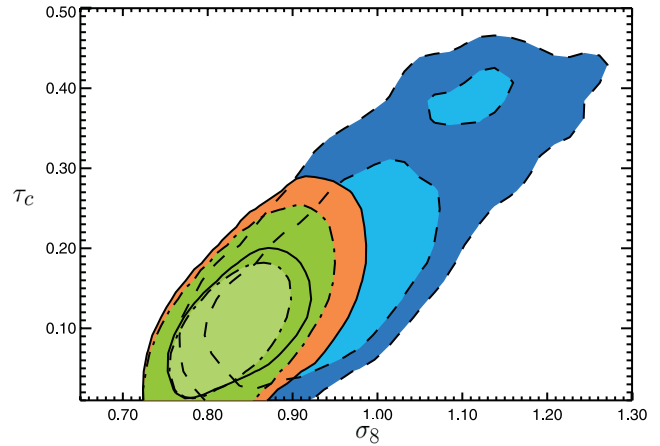
and Sloan Digital Sky Survey (Tegmark et al. 2004) results for the shape of the matter power spectrum than the direct application of the 2dfGRS data gives. Explicitly the prior on the amplitude is $\sigma_8 \Omega_m^{0.56} = 0.47^{+0.02,+0.11}_{-0.02,-0.08}$, distributed as a Gaussian (first error) convolved with a uniform (top-hat) distribution (second error), both in $\ln(\sigma_8 \Omega_m^{0.56})$. The prior on the effective shape parameter is $\Gamma_{\rm eff} = 0.21^{+0.03,+0.08}_{-0.03,-0.08}$. Again the small-scale CMB results substantially improve the constraints in comparison to what is obtained with only the larger angular scale CMB data. Figure 9 shows the τ_C-σ_8 plane, illustrating the exclusion of the high values along the line of near-degeneracy that results when CBI and ACBAR data are added to *WMAP*+LSS.

All of the above analysis assumes $\Omega_{\rm tot} = 1$. It is well known that revoking this assumption yields substantially worse parameter estimates when CMB data are analyzed in isolation (e.g., Efstathiou & Bond 1999; Spergel et al. 2003; Bond et al. 2003; Tegmark et al. 2004 and references therein). The main parameters affected are Ω_m, Ω_Λ, and H_0; typically, low Hubble parameters and larger ages t_0 are favored in this case. For CBI+ALL we find a factor of $\sim$2–3 degradation in the precision of the constraints on Ω_Λ and Ω_m. The best value for the curvature in this scenario is $\Omega_k = -0.052^{+0.037}_{-0.036}$. Results on $\Omega_b h^2$, $\Omega_c h^2$, τ_C, and n_s are not significantly affected.[17] Thus CMB data alone yield a robust determination of the nonbaryonic dark matter density, and a determination of the total baryon content of the universe consistent with those derived from deuterium absorption measurements (Kirkman et al. 2003), as well as limits from other light-element methods (e.g., Bania et al. 2002 and references therein).

4.2. *Running of the Scalar Spectral Index*

Inflation models rarely give pure power laws, with $n_s(k)$ constant, even over the limited ranges of wavenumber k that the CMB+LSS data probe. In most models, the breaking is

[17] This explains the mechanism for degraded estimates of other parameters: increased uncertainty in H_0 coupled with fixed values of $\Omega_b h^2$ and $\Omega_c h^2$ leads to the increased uncertainty in Ω_m, also causing an increased uncertainty in Ω_Λ.

TABLE 5
Cosmological Constraints Including a Running Spectral Index

Parameter	WMAP+LSS	CBI+WMAP+LSS	CBI+ALL+LSS
$\Omega_b h^2$	$0.0249^{+0.0025}_{-0.0025}$	$0.0222^{+0.0019}_{-0.0017}$	$0.0218^{+0.0013}_{-0.0014}$
$\Omega_c h^2$	$0.116^{+0.013}_{-0.013}$	$0.120^{+0.013}_{-0.012}$	$0.124^{+0.011}_{-0.011}$
Ω_Λ.....................................	$0.74^{+0.08}_{-0.08}$	$0.69^{+0.08}_{-0.08}$	$0.67^{+0.07}_{-0.07}$
τ_C	$0.32^{+0.08}_{-0.07}$	$0.24^{+0.05}_{-0.07}$	$0.21^{+0.03}_{-0.06}$
n_s	$1.0^{+0.08}_{-0.08}$	$0.90^{+0.06}_{-0.06}$	$0.88^{+0.05}_{-0.05}$
α_s	$-0.061^{+0.037}_{-0.037}$	$-0.085^{+0.031}_{-0.030}$	$-0.087^{+0.028}_{-0.028}$
$10^{10}A_S$..................................	$36.1^{+10.0}_{-10.0}$	$29.4^{+7.1}_{-6.4}$	$28.1^{+5.3}_{-5.2}$
H_0	$75.7^{+9.2}_{-8.7}$	$68.9^{+7.1}_{-6.2}$	$67.0^{+5.2}_{-5.1}$
Age (Gyr)............................	$13.2^{+0.5}_{-0.5}$	$13.7^{+0.3}_{-0.4}$	$13.8^{+0.2}_{-0.3}$
Ω_m..	$0.26^{+0.08}_{-0.08}$	$0.31^{+0.08}_{-0.08}$	$0.33^{+0.07}_{-0.07}$
σ_8...	$1.0^{+0.1}_{-0.1}$	$0.92^{+0.08}_{-0.08}$	$0.91^{+0.07}_{-0.07}$

NOTES.—Cosmological constraints including a running spectral index $\alpha_s = dn_s/d \ln k$ obtained from the CMB and our conservative LSS prior. We find all combinations prefer a negative value for α_s with significances above the 2 σ level for the combinations CBI+WMAP and CBI+ALL.

rather gentle, with small corrections having been entertained since the early eighties. Much more radical forms for $n_s(k)$ are possible. The gentle form most often adopted involves a running index described by a logarithmic correction:

$$n_s(k) \equiv \frac{d \ln P}{d \ln k} = n_s(k_0) + \alpha_s \ln\left(\frac{k}{k_0}\right), \qquad (2)$$

where $\alpha_s = dn_s/d \ln k$. Here $P(k)$ is the primordial post-inflation power spectrum for scalar curvature perturbations and k_0 is a pivoting scale about which $n_s(k)$ is expanded. The effect is that for negative α_s the slope is flattened below k_0 and steepened above k_0, i.e., power is suppressed on scales both greater than and less than k_0.

There has been much focus recently on whether the data require such a running index, motivated by the incorporation of Lyα absorption data in the WMAP analyses of Spergel et al. (2003), and explored further by, e.g., Bridle et al. (2003), Bastero-Gil et al. (2003), and Mukherjee & Wang (2003). Bond et al. (2003) have shown that the CMB data marginally favor a nonvanishing negative running term. The effect is driven by the requirement to reconcile an apparent lack of power on the largest scales observed by WMAP with observations on arc-minute scales such as those reported in this work. In this regard, CBI adds a significant lever arm beyond WMAP to higher l, and the CBI/WMAP cross-calibration presented here therefore helps to further constrain the allowed variation of $n_s(k)$.

Table 5 shows the parameters we obtain when our basic parameter set is expanded to include a running term $\alpha_s = dn_s/d \ln k$, with the LSS prior applied for the three cases. We have not limited α_s by any theoretical prior prejudices, but have just allowed it to vary over the range $-0.2 < \alpha_s < 0.2$. The final one-dimensional marginalized distributions for a number of combinations of data and priors are shown in Figure 10. Analyzing the WMAP data alone, we find $\alpha_s = -0.077^{+0.044}_{-0.086}$; including the CBI results favors a more negative value $\alpha_s = -0.105^{+0.036}_{-0.038}$. Adding LSS constraints reduces the uncertainties somewhat, yielding $\alpha_s = -0.085^{+0.031}_{-0.030}$. Estimates for the optical depth τ_C and linear amplitude σ_8 are generally higher and those for the spectral index at the chosen pivot scale $n_s(k_0 = 0.05$ Mpc$^{-1})$ are lowered. Figure 11 shows the σ_8-α_s marginalized distribution for three data combinations. We note that α_s is significantly correlated with other cosmo-logical parameters, in particular with $n_s(k_0)$, τ_C, and σ_8, so

applying further priors to α_s motivated by inflation theory would affect these results, but it is useful to see what the data imply without such impositions.

4.3. Constraints on σ_8 from the High-l Excess Power

Intrinsic CMB anisotropies on small angular scales are expected to be significantly suppressed by photon viscosity and the finite thickness of the last scattering region. Data from the CBI were the first to show this damping tail by mapping a drop of more than a factor of 10 in power between $l = 400$ and $l = 2000$. This damping has subsequently also been observed by both ACBAR and the VSA.

A number of effects are expected to produce secondary anisotropies which peak at high l. These include the Vishniac effect (Vishniac 1987), gravitational lensing (Blanchard & Schneider 1987), patchy reionization (Aghanim et al. 1996), the Sunyaev-Zeldovich effect in galaxy clusters at moderate
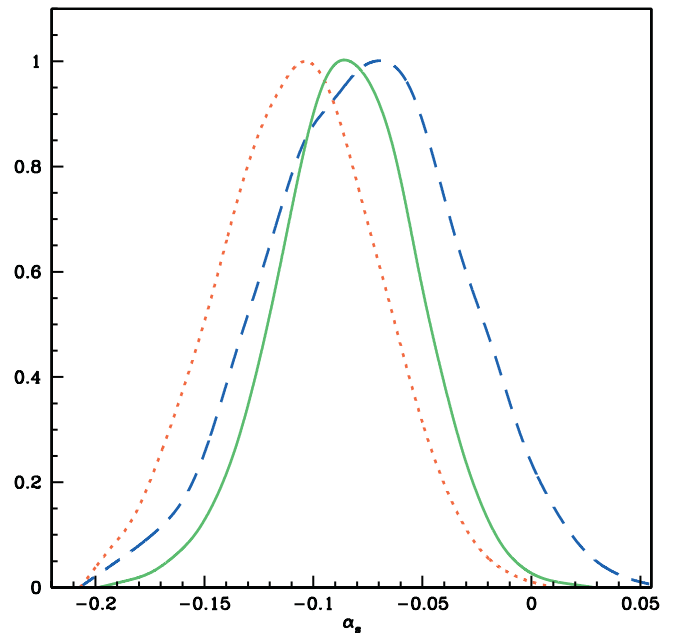

FIG. 10.—Marginalized distributions for the running spectral index parameter α_s defined in eq. (2). The blue dashed curve is for "WMAP only," and the red dotted curve is for "CBI+WMAP" (both for the flat plus weak-h prior case). The green solid curve shows the result when also including our LSS prior.
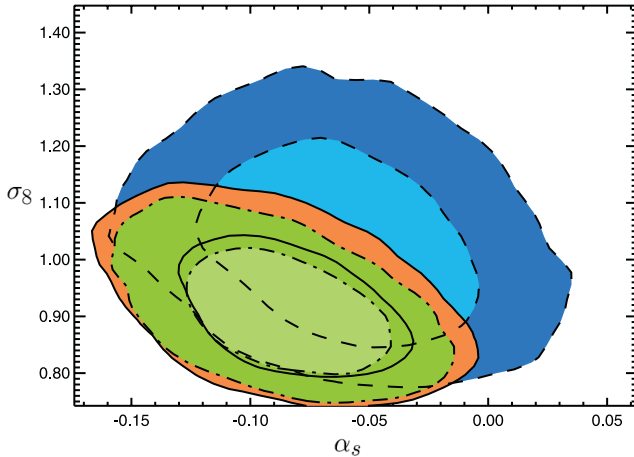
FIG. 11.—Marginalized two-dimensional distributions for the running spectral index parameter α_s and amplitude σ_8. Shown are the 1 and 2 σ constraints from "*WMAP* only" (*dashed lines delineating the blue region*); "*WMAP*+CBI" (*solid delineating the orange region*) both for the flat plus weak-*h* prior case. The dash-dotted lines delineating the green regions show the results for the "CBI+ALL" case with the LSS prior also included. As in Fig. 9, only data at $l < 2000$ are used.

redshifts $z \lesssim 5$ (e.g., Bond & Myers 1996; Cooray 2001), and Sunyaev-Zeldovich fluctuations from the first stars at high redshifts ($z \sim 20$) (Oh et al. 2003).

We previously considered the possible implications of the SZE in galaxy clusters at moderate redshifts (Bond et al. 2004), and here we discuss this effect in the light of the new results presented above. We have estimated σ_8 by fitting jointly for a primary CMB spectrum and template SZE spectra. The technique is detailed in Goldstein et al. (2003), where a combination of high-*l* band powers (Mason et al. 2003; Kuo et al. 2004; Dawson et al. 2002) was used in a two parameter fit of "primary" and "secondary" spectrum amplitude parameters. The SZE contribution to the power spectrum is highly dependent on the amplitude of the mass fluctuations, characterized by σ_8 (e.g., Komatsu & Kitayama 1999; Seljak et al. 2001; Bond et al. 2004). Since the SZE power spectrum has a weak dependence on Ω_b in addition to a strong σ_8 dependence, it is useful to use an amplitude parameter σ_8^{SZ} to describe the scaling of the secondary SZE power spectrum. Assuming that the power spectrum C_l^{SZ} scales as $(\Omega_b h)^2 \sigma_8^7$, we define $\sigma_8^{\mathrm{SZ}} \equiv (\Omega_b h / 0.035)^{2/7} \sigma_8$. It should be noted that secondary anisotropies, unlike intrinsic anisotropies, are not expected to have a Gaussian distribution. Although the detections in these bands are marginal, the strong dependence of the SZE power spectrum on the linear amplitude of the matter power spectrum already implies some constraints on the value of σ_8. The primary spectrum amplitude parameter encompasses the linear

amplitude of perturbations, as well as the effects of n_s and τ_C on the expected high-*l* band power. Goldstein et al. (2003) present an extensive discussion of the fitting procedure.

The method approximates the effect of the non-Gaussian secondary anisotropy power spectra by multiplying the expected sample variance in each band by a factor f_{NG} of between 1 and 4. The bin covariances are increased by the same factor. While this approach is simplistic, it is supported by numerical simulations that have shown the variance of simulated power spectra to be greater than the Gaussian case by a factor of approximately 3 for the *l*-range considered (Cooray 2001; White et al. 2002; Komatsu & Seljak 2002; Zhang et al. 2002). Future work may require a more accurate treatment of non-Gaussianity. However, we note that even large changes ($f_{\mathrm{NG}} = 1$–4) have a minimal impact on the results. There are also theoretical uncertainties of a factor of $\sim$2 in the theoretical SZE power spectrum predictions. These theoretical uncertainties translate into $\sim$10% in σ_8 and are also a limiting factor.

For this work we used the last two bands of the power spectrum in the "even" binning of Table 1 for the CBI results, the last three bands of the ACBAR results (Kuo et al. 2004), and the two band result from the BIMA array (Dawson et al. 2002). As a template primary spectrum we used the best-fit ΛCDM model with power-law initial spectrum to the *WMAP* data.[18] We assign a Gaussian prior with an rms of 10% around the best-fit amplitude for the primary spectrum while keeping all other parameters fixed, and marginalize over the primary amplitude parameter when deriving the final confidence intervals for σ_8^{SZ}. We have also included, for the CBI band powers, uncertainties due to the residual discrete source and thermal noise corrections. By considering the χ^2 of the CBI+ACBAR+BIMA to a model comprising primary anisotropy and zero SZE signal, and with $f_{\mathrm{NG}} = 1$, we associate a statistical significance of 98% with the detection of an SZE foreground at $l > 2000$. The BIMA+CBI data alone give a 92% significance.

In Table 6 we show the constraints on σ_8^{SZ} obtained from the fits to CBI+BIMA and to CBI+BIMA+ACBAR. The distributions have long tails extending to low values of σ_8^{SZ} and are effectively unbounded from below (see Fig. 12). In the context of our calculation, this is entirely due to Gaussian statistics and the results of changing variables to band power$^{1/7}$ (in effect). We therefore define the confidence intervals as centered around the maximum in the distribution with the 1 σ bounds given by a drop of a factor of $e^{-1/2}$ on either side.

We note that the results we derive for σ_8^{SZ} are rather similar to those obtained using the 1 yr deep CBI field in conjunction with BIMA and ACBAR, as reported by Goldstein et al. (2003). We have repeated this analysis of the CBI one-year

[18] See http://lambda.gsfc.nasa.gov.

TABLE 6
VALUES OF σ_8^{SZ}

Experiments	$f_{\mathrm{NG}} = 1$	$f_{\mathrm{NG}} = 2$	$f_{\mathrm{NG}} = 3$	$f_{\mathrm{NG}} = 4$
CBI+BIMA	$0.96^{+0.07}_{-0.08}$	$0.96^{+0.07}_{-0.09}$	$0.96^{+0.07}_{-0.10}$	$0.96^{+0.07}_{-0.11}$
CBI+BIMA+ACBAR	$0.98^{+0.06}_{-0.07}$	$0.98^{+0.06}_{-0.07}$	$0.98^{+0.06}_{-0.07}$	$0.98^{+0.06}_{-0.08}$

NOTES.—σ_8^{SZ} values derived from the marginalized distributions obtained by fitting an SZE spectrum to the high-*l* CMB data. The value for f_{NG} is the factor used in rescaling the sample variance for each band (and interband correlations) to approximate varying degrees of non-Gaussianity. We find that the confidence limits do not depend strongly on the assumed f_{NG}.
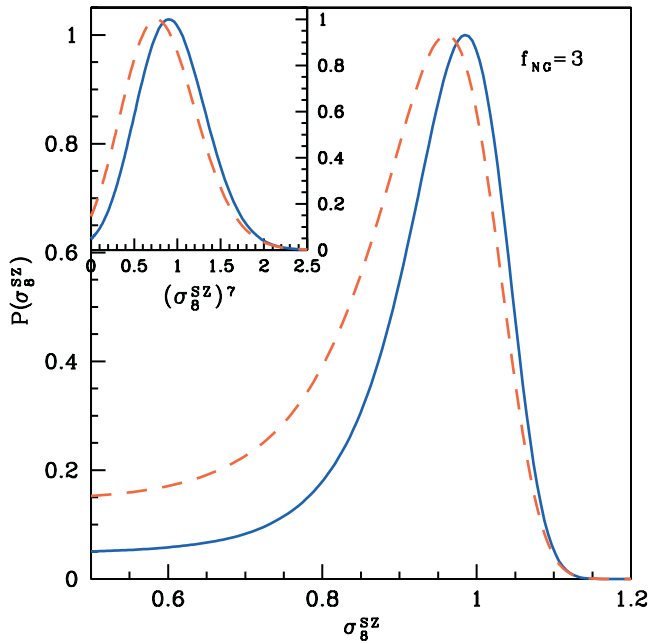
Fig. 12.—Constraints on secondary SZE anisotropy, as parameterized by the effective parameter σ_8^{SZ}. The curves are obtained from fits to the data at $l > 2000$ (CBI and BIMA [*red dashed line*], and CBI, BIMA, and ACBAR [*blue solid line*]). The fitting accounts for a separate contributions from template primary and secondary spectra. The marginalized distribution is heavily skewed toward low σ_8^{SZ} values because of the assumed scaling of the secondary signal. In the inset we have plotted the distribution against $(\sigma_8^{SZ})^7$ to show how the distribution is approximately Gaussian in this variable, which roughly corresponds to the high-l band power in a given experiment.

deep field results using the cross-calibration with *WMAP*, and find similar results. This is because the deep field component of our combined two-year data dominates the high-l power, and this is not changed much when the extra deep field 2001 data are added. What is important to note is that the much larger spatial coverage afforded by the full mosaic data set (and thereby lesser sample variance) does not much diminish the amplitude of σ_8^{SZ}.

5. CONCLUSIONS

The CBI power spectrum is compared with *WMAP* and ACBAR results in Figure 13. These results, together with those from a host of other ground- and balloon-based experiments in recent years, are consistent with the key predictions of structure formation and inflationary theories: The universe is close to flat; the initial spectrum of perturbations is nearly scale-invariant; oscillations and damping in the power spectrum evince the expected signatures of subhorizon-scale causal processes; initial conditions are Gaussian and are consistent with adiabatic fluctuations; and the magnitude of fluctuations from the largest scales down to galaxy cluster scales is consistent with what is needed to produce locally observed structures through gravitational collapse. For discussion of these points, see Bond et al. (2002), Peiris et al. (2003), and references therein. The concordance of observational results with theoretical expectations has permitted cosmological parameters to be determined with precision. In this work we obtain $\Omega_b h^2 = 0.0225^{+0.0009}_{-0.0009}$, $\Omega_c h^2 = 0.111^{+0.010}_{-0.009}$, $\Omega_\Lambda = 0.74^{+0.05}_{-0.04}$, $\tau_C = 0.11^{+0.02}_{-0.03}$, $n_s = 0.95^{+0.02}_{-0.02}$, $t_0 = 13.7^{+0.2}_{-0.2}$ Gyr, and $\Omega_m = 0.26^{+0.04}_{-0.05}$ from a selection of current primary anisotropy data including CBI, *WMAP*, ACBAR,
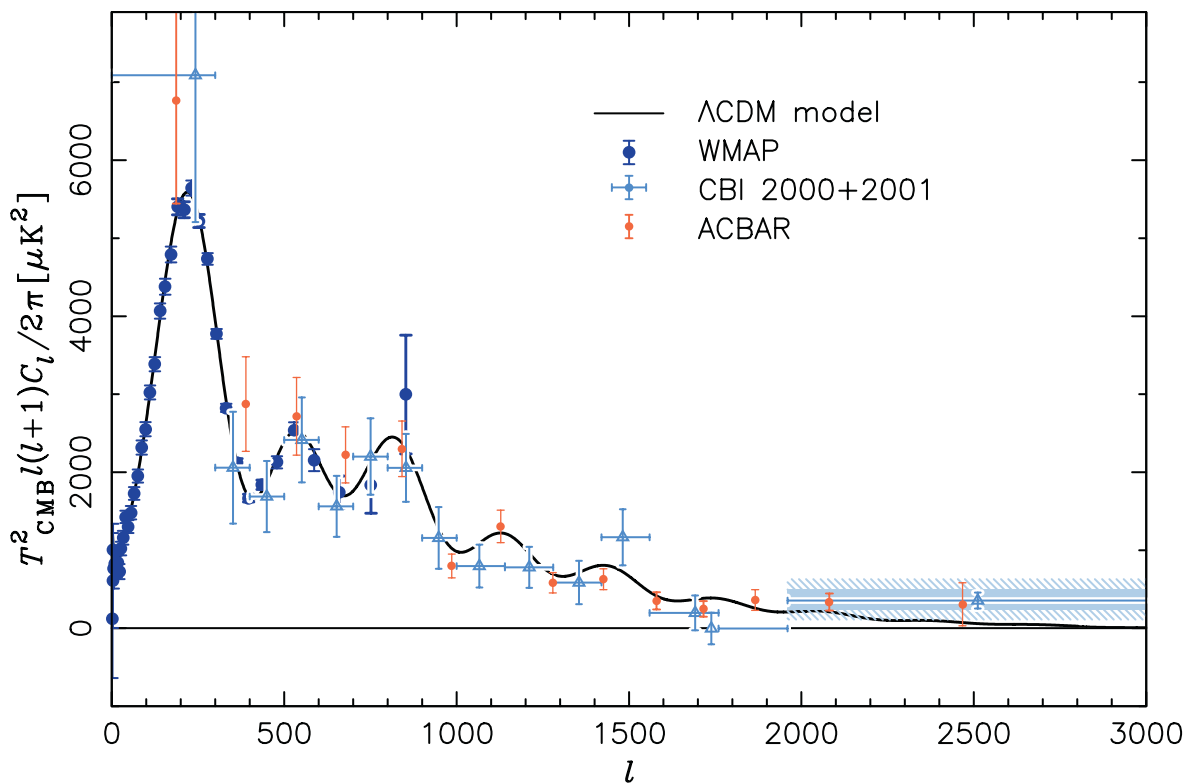

Fig. 13.—CBI+*WMAP*+ACBAR Spectrum. The solid black line is the *WMAP* ΛCDM model with a pure power-law primordial spectrum (wmap_lcdm_pl_model_yr1_v1.txt). The highest l ACBAR point has been displaced slightly to lower l for clarity. The blue shaded and hatched regions indicate the 1 and 2 σ confidence intervals on the high-l CBI measurement.

and BOOMERANG, and using the flat plus weak-h prior (see Table 3). Similar results are obtained when large-scale structure priors are incorporated (Table 4). As discussed in § 4 a flat prior (i.e., assumption that $\Omega_{tot} = 1$) is imposed on most of our parameter analysis; while supported by observational data, this does impose a strong constraint, and some parameter estimates would be less accurate without it. A marginal detection of a running scalar spectral index remains and is consistent with that presented by Spergel et al. (2003).

As discussed in § 4.1, the addition of CMB data from $600 < l < 2000$ significantly improves constraints on $\Omega_b h^2$, n_s, the amplitude of the primary anisotropies, the age of the universe, and τ_C relative to what is obtained with only large-scale CMB data (see Fig. 7). In the absence of a restrictive τ_C prior the $l < 600$ data leave significant degeneracies that are broken by the higher l experiments (see Figs. 8 and 9). We note that the improvement between the "CBI+WMAP" and "CBI+ALL" cases comes primarily from the addition of the BOOMERANG data. Improvements are also seen in analyses which allow a running scalar spectral index (Fig. 11). The tight constraint on the baryon density, $\Omega_b h^2 = 0.0225^{+0.0009}_{-0.0009}$ compares favorably with observationally determined BBN values of $\Omega_b h^2 = 0.0214 \pm 0.0020$ (Kirkman et al. 2003). We have also obtained an accurate measurement of n_s from the CMB data only, $n_s = 0.95 \pm 0.02$. These results are robust with respect to prior assumptions, such as flatness, imposed on the analysis. By way of comparison the WMAP-only values for these parameters are $\Omega_b h^2 = 0.0243 \pm 0.0016$ and $n_s = 1.01 \pm 0.05$. The breaking of these degeneracies largely relies on the ratio of power levels on small angular scales to those on large angular scales, so the precision of these results has benefited from the accurate cross-calibration with WMAP. The CBI data also favor a negative running scalar spectral index $\alpha_s = -0.087 \pm 0.028$ (CBI+ALL+LSS), consistent with the results from WMAP combined with LSS constraints

In Figure 14 we show the same data as plotted in Figure 13, now on a log-log plot and with additional curves which show the expected level of SZE power for the two sets of simulations discussed by Bond et al. (2004). Note that the fortuitous "agreement" between the CBI and ACBAR power levels at $l > 2000$ is not expected if the power has a significant component due to the Sunyaev-Zel'dovich effect because of the different observing frequencies. Nevertheless, given the uncertainties in these two measurements, it can be seen that the models span a range of power at high l that fits both the CBI and ACBAR observations.

The detection of power at $l > 2000$ is consistent with the results presented by Mason et al. (2003), although somewhat lower. We find a band power 355^{+137}_{-122} μK^2 (68% confidence, including systematic contributions). By combining this result with high-l results from BIMA and ACBAR, we detect power in excess of that expected from primary anisotropy at 98% confidence. This result includes a marginalization over expected primary anisotropy power levels. Assuming the signal in excess of expected primary anisotropy is due to a secondary SZ foreground we determine $\sigma_8^{SZ} = 0.96^{+0.06}_{-0.07}$ (68%). The lower confidence level of the detection of an excess, and also the smaller values of σ_8^{SZ}, are chiefly due to the lower high-l band power we obtain and the inclusion of the uncertainty in the primary anisotropy band power at $l > 2000$. The strong dependence of the observable power on σ_8 gives rise to firm upper limits on σ_8 but a tail to low values (Fig. 12). It should be borne in mind that there are systematic uncertainties in the theoretical prediction of the power spectrum due to secondary
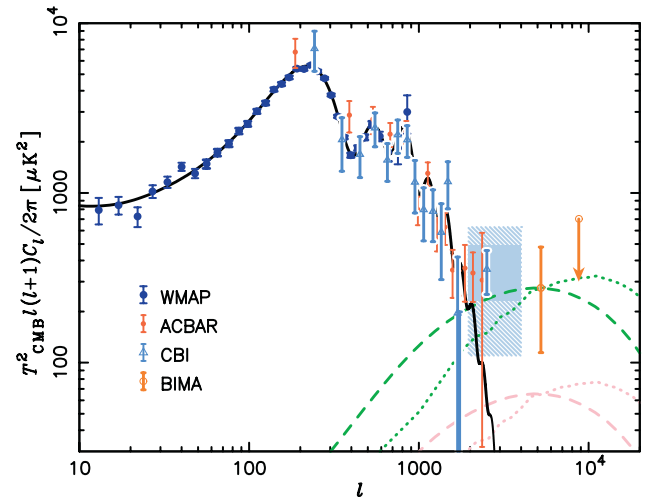

FIG. 14.—CBI+WMAP+ACBAR Spectrum+high-l points from BIMA. The curves at high l show the levels of SZ power expected in representative models using moving mesh hydrodynamics simulations (*dotted line*) and smooth particle hydrodynamics (*dashed line*) simulations (see text). The green and pink curves correspond to 30 and 150 GHz, respectively. In these simulations $\sigma_8^{SZ} = 0.98$, which also fits well the WMAP and CBI observations at lower l for the case of a running spectral index (see Table 5). The highest l ACBAR point has been displaced slightly to lower l for clarity.

SZ anisotropies that correspond to a 10% systematic uncertainty in σ_8.

An appreciable fraction of CBI data were rejected by vetoing NVSS sources, and furthermore the uncertainty in the power level of the source population remaining after the NVSS veto is a limiting factor at $l > 2000$. In late 2004 a sensitive, wide-band continuum receiver will be commissioned on the Green Bank Telescope (GBT) to deal with both of these issues. This will result in a more sensitive determination of the total intensity power spectrum at all l covered by the CBI. Since the end of the observations reported here, the CBI was upgraded and dedicated to full-time polarization observations.

REFERENCES

Aghanim, N., Desert, F. X., Puget, J. L., & Gispert, R. 1996, A&A, 311, 1
Bania, T. M., Rood, R. T., & Balser, D. S. 2002, Nature, 415, 54
Bastero-Gil, M., Freese, K., & Mersini-Houghton, L. 2003, Phys. Rev. D, 68, 123514
Bennett, C. L., et al. 2003, ApJS, 148, 97
Blanchard, A., & Schneider, J. 1987, A&A, 184, 1
Bond, J. R., Contaldi, C. R., & Pogosyan, D. 2003, Philos. Trans. R. Soc. London A, 361, 2435
Bond, J. R., Jaffe, A. H., & Knox, L. 1998, Phys. Rev. D, 57, 2117
Bond, J. R., & Myers, S. T. 1996, ApJS, 103, 63
Bond, J. R., et al. 2002, in AIP Conf. Ser. 646, Theoretical Physics: MRST 2002: A Tribute to George Leibbrandt, ed. V. Elias, R. J. Epp, & R. C. Myers (Melville: AIP), 15
———. 2004, ApJ, submitted (Paper VI)
Bridle, S. L., Lewis, A. M., Weller, J., & Efstathiou, G. 2003, MNRAS, 342, L72
Condon, J. J., Cotton, W. D., Greisen, E. W., Yin, Q. F., Perley, R. A., Taylor, G. B., & Broderick, J. J. 1998, AJ, 115, 1693
Cooray, A. 2001, Phys. Rev. D, 64, 063514
Dawson, K. S., et al. 2002, ApJ, 581, 86
de Bernardis, P., et al. 2000, Nature, 404, 955
Dickinson, C., et al. 2004, MNRAS, submitted (astro-ph/0402498)
Efstathiou, G., & Bond, J. R. 1999, MNRAS, 304, 75
Goldstein, J. H., et al. 2003, ApJ, 599, 773
Grainge, K., et al. 2003, MNRAS, 341, L23
Griffiths, L. M., Kunz, M., & Silk, J. 2003, MNRAS, 339, 680
Halverson, N. W., et al. 2002, ApJ, 568, 38
Kirkman, D., Tytler, D., Suzuki, N., O' Meara, J., & Lubin, D. 2003, ApJS, 149, 1
Komatsu, E., & Kitayama, T. 1999, ApJ, 526, L1

Komatsu, E., & Seljak, U. 2002, MNRAS, 336, 1256
Kuo, C. L., et al. 2004, ApJ, 600, 32
Lee, A. T., et al. 2001, ApJ, 561, L1
Lewis, A., & Bridle, S. 2002, Phys. Rev. D, 66, 103511
Mason, B. S., Leitch, E. M., Myers, S. T., Cartwright, J. K., & Readhead, A. C. S. 1999, AJ, 118, 2908
Mason, B. S., et al. 2003, ApJ, 591, 540 (Paper II)
Miller, A. D., et al.1999, ApJ, 524, L1
Mukherjee, P., & Wang, Y. 2003, ApJ, 599, 1
Myers, S. T., et al. 2003, ApJ, 591, 575 (Paper IV)
Netterfield, C. B., et al. 2002, ApJ, 571, 604
Oh, S. P., Cooray, A., & Kamionkowski, M. 2003, MNRAS, 342, L20
Padin, S., et al. 2001, ApJ, 549, L1 (Paper I)
———. 2002, PASP, 114, 83
Page, L., et al. 2003, ApJS, 148, 39
Pearson, T. J., et al. 2003, ApJ, 591, 556 (Paper III)
Peiris, H. V., et al. 2003, ApJS, 148, 213
Percival, W. J., et al. 2002, MNRAS, 337, 1068
Ruhl, J., et al. 2003, ApJ, 599, 786
Scott, P. F., et al. 2003, MNRAS, 341, 1076
Seljak, U., Burwell, J., & Pen, U. 2001, Phys. Rev. D, 63, 063001
Sievers, J. L. 2003, Ph.D. thesis, Caltech
Sievers, J. L., et al. 2003, ApJ, 591, 599 (Paper V)
Spergel, D. N., et al. 2003, ApJS, 148, 175
Subramanian, K., Seshadri, T. R., & Barrow, J. D. 2003, MNRAS, 344, L31
Tegmark, M., et al. 2004, Phys. Rev. D, 69, 103501
Vishniac, E. T. 1987, ApJ, 322, 597
White, M., Hernquist, L., & Springel, V. 2002, ApJ, 579, 16
Zhang, P., Pen, U., & Wang, B. 2002, ApJ, 577, 555